Building pore pressure and rock physics guides to constrain anisotropic waveform inversion

Huy Le, Anshuman Pradhan, Nader Dutta, Biondo Biondi, Tapan Mukerji, and Stewart A. Levin

ABSTRACT

We developed a workflow that combines various sources of information, such as geomechanics, well logs, basin history, and diagenesis, to model pore pressure-velocity relation based on rock physics principles. Our workflow produces velocity templates, which can be used as constraints in any anisotropic waveform inversion process. We apply our workflow to a data set from the Gulf of Mexico. We study the diagenesis of shale, particularly, smectite-illite reaction. From well logs, we build models for velocity-porosity and density-overburden relations. Thermal history is approximated from available Bottom Hole Temperature (BHT) data and depositional history is inferred from interpreted horizons. We use mud weight data to calibrate our pore pressure-velocity transformation. A number of different pore pressure gradient scenarios result in different velocity profiles or templates. Combining with mud weight data, these templates provide bound constraints to waveform inversion. The integration and calibration of many sources of data in our workflow ensure the resulting velocity model is geologically feasible physically plausible.

INTRODUCTION

Anisotropic imaging has been shown to be necessary in many successful exploration applications, particularly in the Gulf of Mexico. Alignment of clay minerals in shales and the effect of layering both imply transverse isotropy. Additionally, salt bodies in the Gulf of Mexico can cause stress perturbations that further complicate velocity variation.

Building anisotropic velocity models for imaging is a challenge due to large uncertainties in anisotropic parameters. Conventional velocity analysis and tomography of surface seismic usually do not provide a satisfactory answer because a number of models could equally well explain the observed data. Such is also the case with full waveform inversion (FWI). All of these inversion schemes rely heavily on the assumption that the initial model is close to the true model. When this assumption does not apply, there is a high possibility of obtaining a velocity model that satisfies the imposed convergence criterion but may be geologically and physically improbable.

Our workflow imposes constraints that not only satisfy the gather flattening criterion but also require the model to be geologically and physically possible.

Anisotropic velocity models can be built with forward modeling using rock physics principles, geomechanics, and basin modeling. Bachrach (2010) used differential effective medium (DEM) theory from rock physics combined with well logs and empirical models of shale diagenesis to build anisotropic velocity models. Petmecky et al. (2009) derived anisotropic velocities for imaging from a 3D basin modeler to capture the pressure, depositional, fluid flow, and salt movement histories of a basin. Matava et al. (2016) used finite elastic deformation theory to calculate the effect of stress anomalies caused by salt movements on velocity.

Recent developments in anisotropic velocity model building show that integrating additional data, such as rock physics and pore pressures, can constrain the velocity inversion process. Dutta et al. (2015) combined rock physics and pore pressure-velocity models to create velocity bounds for tomography. These constraints not only reduce uncertainty in the tomography process, but also produce a velocity model that is able to predict physical pore pressure. This is an extra constraint that forces the vertical velocity to be within a physically expected range such as yielding a pore pressure that is bounded below by hydrostatic pore pressure and above by fracture pressure. In addition, the use of rock physics compliant velocity model enables us to estimate vertical velocity without having to rely on normal moveout analysis, which often produce poor estimates of velocity. For a review on geopressure prediction, refer to Dutta (2002). Li et al. (2016) used stochastic rock physics modeling (Bachrach, 2010) to build model covariance matrices to constrain wave equation migration velocity analysis (WEMVA). Following Dutta et al. (2015), in this paper, we present a workflow that combines rock physics, basin modeling, and pore pressure constraints to improve anisotropic full waveform inversion (FWI).

WORKFLOW

Conceptual model

Our rock physics workflow applies to the diagenesis of shale, specially, the transformation of smectite into illite as a result of burial diagenesis. Our rock model consists of, therefore, a matrix solid (smectite and illite), and a pore fluid (water). Two processes can affect pore pressure. First, as sediments deposit, mechanical compaction causes porosity to reduce. Second, when clayey rocks are buried to deeper depths and temperature reaches activation temperatures, the transformation from smectite to illite happens and is accompanied by an additional release of water that is bound in the clay system of the host rocks, resulting in further increase in pore pressure.

In our workflow, we define forward modeling as obtaining vertical velocity models from pore pressures. First, effective stress is calculated for various pore pressure gradient scenarios by subtracting pore pressure from overburden stress. Second, effec-

tive stress is then converted into porosity using a compaction-diagenetic model. Finally, porosity is used to compute velocity via an attribute model, a velocity-porosity transformation. Our forward modeling produces velocity templates corresponding to different pore pressure gradients. These templates, when combined with mud weight data, serve as a guide to our inversion process. In the reverse direction, our workflow generates pore pressure predictions from an input of velocity.

Compaction-diagenetic model

Porosity is reduced due to mechanical loading. When loading is slow enough that pore fluid is allowed to escape, pore pressure maintains in a hydrostatic equilibrium. This process is called normal compaction. In this mode, velocity increases as porosity decreases. When loading is faster than the rate of fluid escape, abnormal pressure builds up in the pores, causing effective stress to drop. In this mode of compaction disequilibrium, porosity is reduced at a lower rate than in normal compaction. Changes in porosity due to compaction are described through changes in effective stress.

In shale, diagenesis also affects pore pressure. The transition of smectite to illite, when temperature is high enough, is followed by a release of water. When such water cannot escape, pore pressure further increases and effective stress decreases without significant loss in porosity. We follow Dutta et al. (2014) and Dutta (2016) to model both of these mechanical compaction and diagenetic processes:

$$\sigma = \sigma_0 e^{-\xi\beta}, \tag{1}$$

where:

$$\xi = \frac{\phi}{1-\phi}, \tag{2}$$

and

$$\beta(t) = B_0 N_s(t) + B_1[1 - N_s(t)], \tag{3}$$

with:

$$N_s(t) = N_0 e^{-\int_0^t A e^{\frac{-E}{RT(t)}} dt}. \tag{4}$$

In the above equations, σ is effective stress and σ_0 is the effective stress necessary to reduce porosity, ϕ, to zero. ξ is the ratio of pore and solid volumes. β is the diagenetic function that characterizes smectite-illite transition. $N_s(t)$ is the smectite fraction at time t and N_0 is such fraction initially. We assume $N_0 = 1$. B_0 and B_1 control the relative importance of smectite and illite in the beta function. T is temperature. A and E are Arrhenius frequency factor and activation energy, respectively (Dutta et al., 2014).

Attribute model

Velocity is inversely proportional to porosity. In our workflow, we use a velocity-porosity relation that was derived in Issler (1992):

$$\triangle\tau = \triangle\tau_m(1-\phi)^{-X}, \tag{5}$$

with $\triangle\tau$ being slowness, $\triangle\tau_m$ being the solid matrix's slowness, and X is the acoustic factor that captures how slowness (and velocity) varies with porosity.

We combine equations 1, 2, and 5 to get an equation of slowness and effective stress:

$$\triangle\tau = \triangle\tau_m \left[1 + \frac{1}{\beta}\ln\left(\frac{\sigma_0}{\sigma}\right)\right]^{-X}. \tag{6}$$

Effective stress is stress applied to the solid matrix and defined as the difference between overburden stress, S, and pore pressure, p:

$$\sigma = S - p. \tag{7}$$

Equations 3, 4, 6, and 7 form a complete transformation from pore pressure to velocity and vice versa.

APPLICATION TO FIELD DATA

We applied our workflow to a data set acquired offshore Gulf of Mexico. We were provided with a surface seismic data, an isotropic velocity obtained from ray-based tomography, migrated images, angle gathers, a number of interpreted horizons, logs and mud weight data from six wells in the area. Figure 1 shows the wells' locations overlaid on a depth slice at two kilometers of the velocity model. Among these six wells, well SS168 has BHT data and well SS187 has a density log. Figure 2a and 2b show the source and receiver locations of the seismic data.

Thermal and depositional histories

In our workflow, the computation of smectite fraction (Equation 4) and beta function (Equation 3) requires a thermal history, $T(t)$. We approximate a simple thermal history of the study area from temperature-depth and age-depth relationships. We used BHT data at well SS168 to build a piece-wise linear temperature profile and assumed a geothermal gradient, α, that did not change in geologic time:

$$T(t) = T_0 + \alpha z(t), \tag{8}$$

where T_0 is the temperature at sea bottom, which can be calculated as a function of latitude and water depth (Beardsmore and Cull, 2001). Figure 3a shows six temperature profiles at our well locations and BHT data at well SS168. We also assume a

constant burial rate, γ, and estimate age-depth relationship from interpreted horizons, Top Pliocene and Top Miocene (Figure 3b):

$$z(t) = \gamma t. \tag{9}$$

Figures 4a and 4b show smectite fractions and beta functions with depth for $B_0 = 6.5$ and $B_1 = 14$. These figures show that smectite-illite transition starts at about 2–2.5 kilometers and ends at about 6–6.5 kilometers.

Overburden stress model

Overburden stress is calculated by:

$$S = S_0 + g \int_0^z \rho(z) dz, \tag{10}$$

where S_0 is the pressure of the water column at sea bottom and $\rho(z)$ is the depth-dependent density. Using data at well SS187, we compare different density models and the corresponding overburden stresses. Specifically, we select only shale data points using a gamma log (Figure 5) and build a diagenetic model for density by least-squares fitting the equation:

$$\rho = (a_s \triangle\tau + b_s) N_s + (a_i \triangle\tau + b_i)(1 - N_s). \tag{11}$$

Here coefficients a_s, b_s, a_i, and b_i describe linear relationships between slowness, $\triangle\tau$, and densities of smectite and illite respectively. Equation 11 can be used to predict density from velocity. Figure 6 shows the fitting result. Data points are color coded by depth, indicating smectite-illite transition as temperature and depth increase (also shown in Figure 4a).

Figure 7a plots Gardner's and diagenetic density models and the actual density log at well SS187. We observe that diagenetic model well captures the low-frequency trend down to four kilometers deep and starts to deviate slightly in deeper sections. Figure 7b shows the comparison of different overburden stress models. Despite a slight difference among density models below four kilometers, overburden stress models well agree with the empirical model (Dutta (2017) private communication):

$$S = az^2 + bz + cz_0, \tag{12}$$

where $a = 0.0000585$, $b = 2.75$, $c = 1.493$, and z_0 is the water depth. Here stress is measured in psi and depth in meter. For simplicity, we will use this empirical model for overburden calculation.

Calibration

In our workflow, a number of important parameters need to be determined:

1. $\triangle\tau_m$ is the matrix's slowness and X is the acoustic formation-factor exponent (Equation 5). Following Issler (1992), we find these two parameters by fitting the sonic transit time and porosity data from well logs. Figure 8 shows the fitting results for different wells. Among five wells used for fitting, well SS160 gives the most reasonable parameters:

$$\begin{aligned} \triangle\tau &= 2.13 \times 10^{-4} \text{ s/m}, \\ X &= 1.97. \end{aligned} \tag{13}$$

   We use these values in our workflow. Other wells' parameters seem either too high or too low.

2. σ_0 is the effective stress that can reduce porosity to zero (Equation 1). B_0 and B_1 determine relative contributions of smectite and illite in beta function (Equation 3). These parameters were chosen so that the sonic converted pore pressures are bounded below by hydrostatic pressure and above by mud weights. Figures 9a, 10a, 11a, 12a, 13a, and 14a show the results for:

$$\begin{aligned} \sigma_0 &= 26000 \text{ psi}, \\ B_0 &= 6.5, \\ B_1 &= 14. \end{aligned} \tag{14}$$

Pore pressures and velocity templates

Figures 9a, 10a, 11a, 12a, 13a, and 14a show the sonic and seismic converted pore pressure profiles together with mud weights, overburden, and fracture stresses at the wells' locations. Here we take fracture stress to be 97% of overburden stress. Figures 9b, 10b, 11b, 12b, 13b, and 14b show the corresponding velocity templates. We observed that the seismic velocities match generally well with the sonic velocities. Additionally, pore pressure profiles show a deviation from hydrostatic pressure at 3-4 kilometers. This deviation in pore pressures is also reflected on the velocity templates by a velocity reduction. Moreover, the depth at which this pressure deviation and velocity reduction happen agrees with where smectite-illite transition starts (Figure 4a).

Well ST143 (Figure 12) and well ST168 (Figure 13) show a sharp decrease in pore pressure and an increase in velocity at about six kilometers. This is caused by the salt bodies that these two wells came in contact with. Salt bodies' generation and movement can lead to stress and velocity anomalies that our current workflow does not address.

CONCLUSIONS

We developed a workflow that produces velocity templates which can be used to guide an anisotropic waveform inversion process. Our workflow uses seismic, well logs, and

geomechanical data to model depositional, thermal histories, and shale diagenesis. Combined with rock physics principles, we build a transformation that can predict pore pressure from velocity. Incorporated as constraints to an waveform inversion, this assures that the inverted velocity model is physically plausible. This is the focus of our ongoing work.

ACKNOWLEDGEMENTS

We would like to thank Schlumberger MultiClient for providing us the seismic data and IHS Energy Log Services Inc. for the well logs.

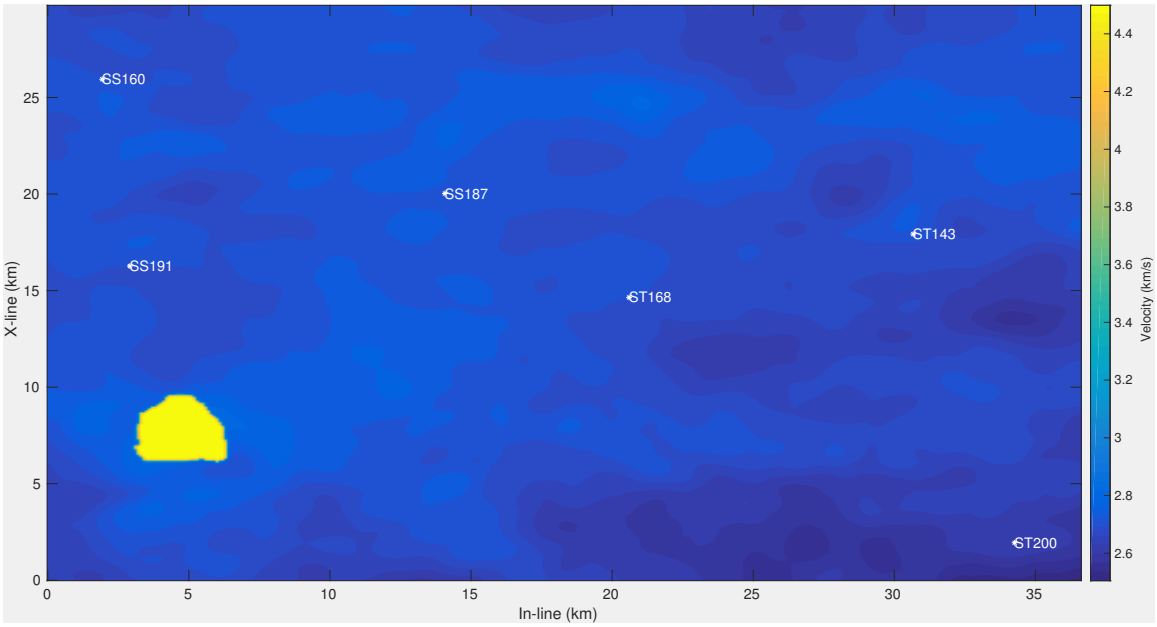

Figure 1: Depth slice at 2 km of the velocity model and well locations. [**ER**]

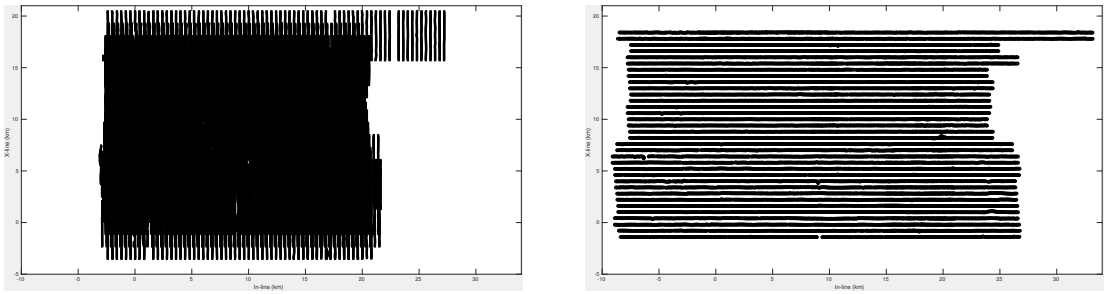

(a) (b)

Figure 2: Source (left) and receiver (right) locations of the provided seismic data. [**ER**]

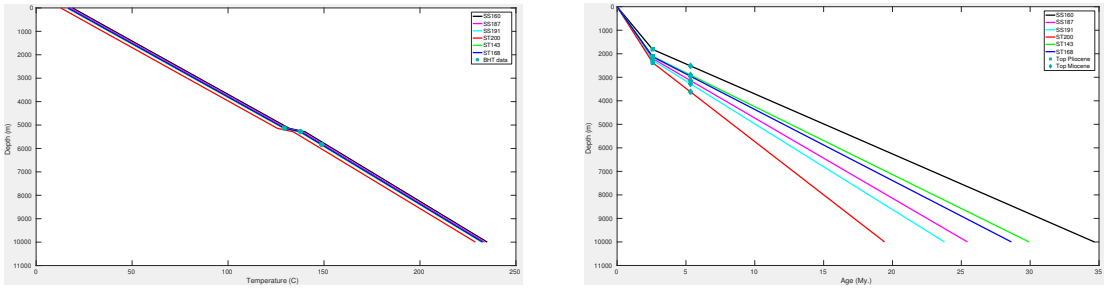

(a) (b)

Figure 3: Temperature-depth (left) and geologic age-depth (right) relationships. [**ER**]

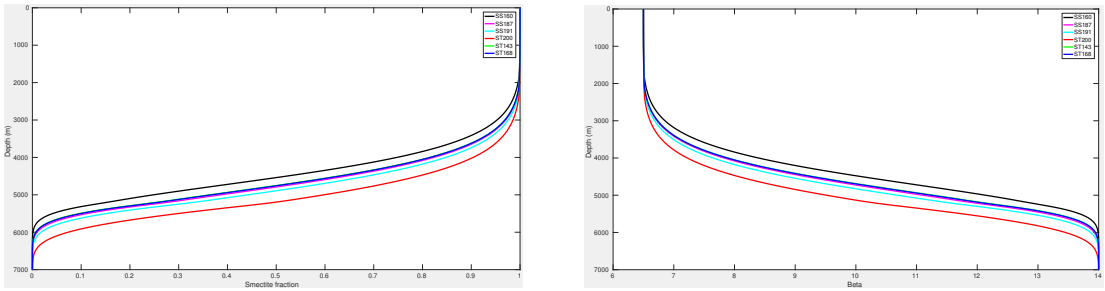

(a) (b)

Figure 4: Smectite fractions (left) and beta functions (right) at well locations. [**ER**]

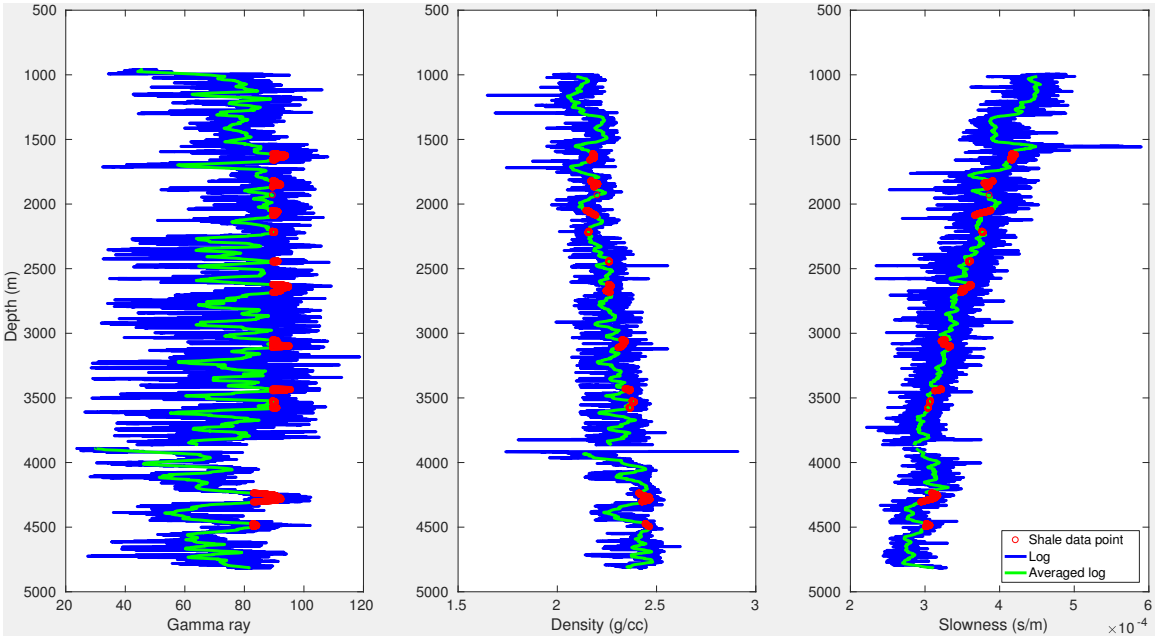

Figure 5: Shale data point selection at well SS187. [**ER**]

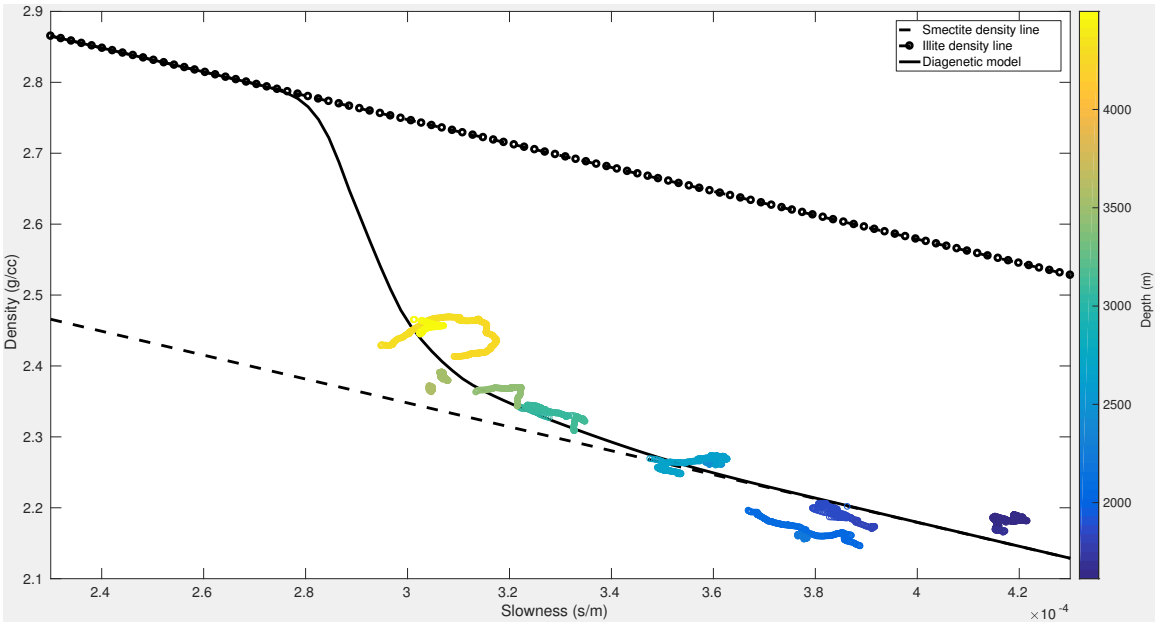

Figure 6: Diagenetic model for density at well SS187. [**ER**]

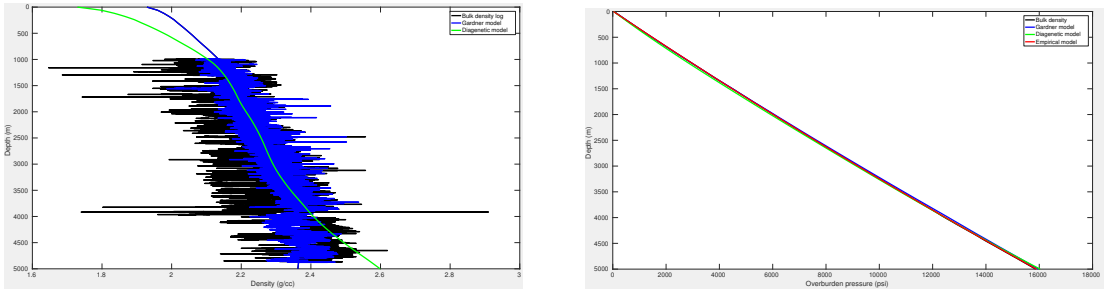

(a) (b)

Figure 7: Different density models (left) and overburden models (right) at well SS187. [**ER**]

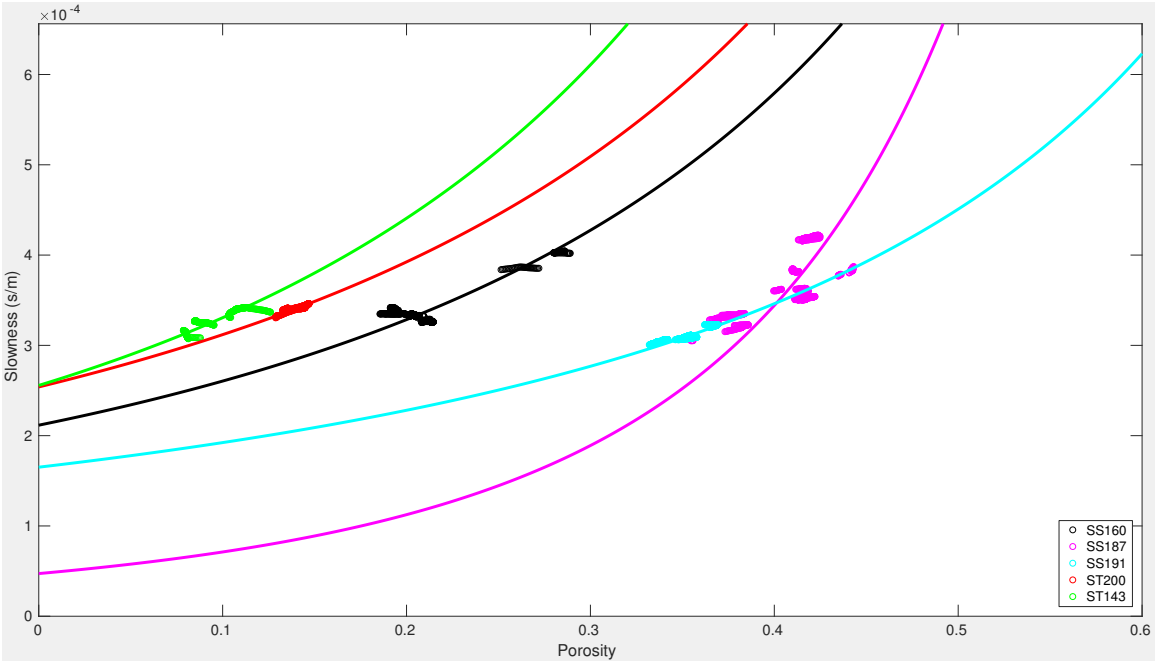

Figure 8: Least-squares fitting for Issler's model. [**ER**]

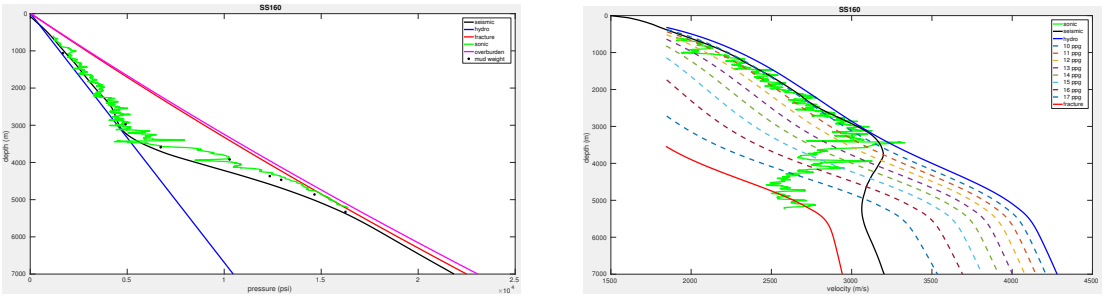

(a) (b)

Figure 9: Pore pressure profile (left) and velocity template (right) at well SS160. [**ER**]

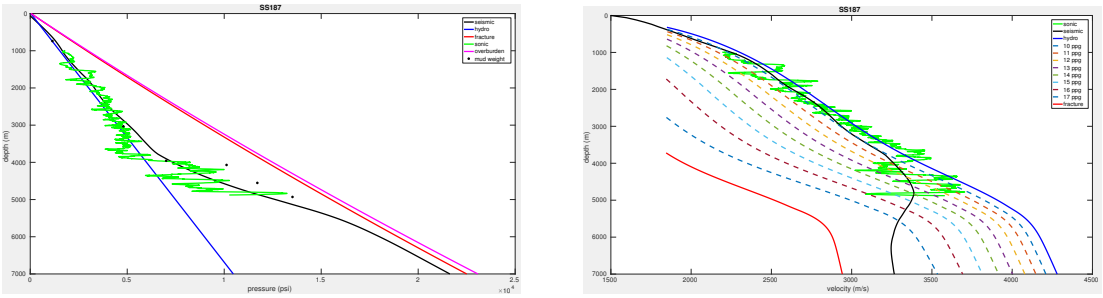

(a) (b)

Figure 10: Pore pressure profile (left) and velocity template (right) at well SS187. [**ER**]

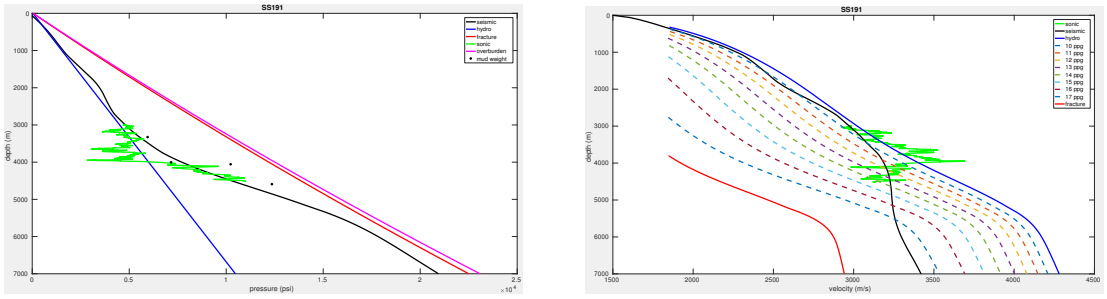

(a) (b)

Figure 11: Pore pressure profile (left) and velocity template (right) at well SS191. [**ER**]

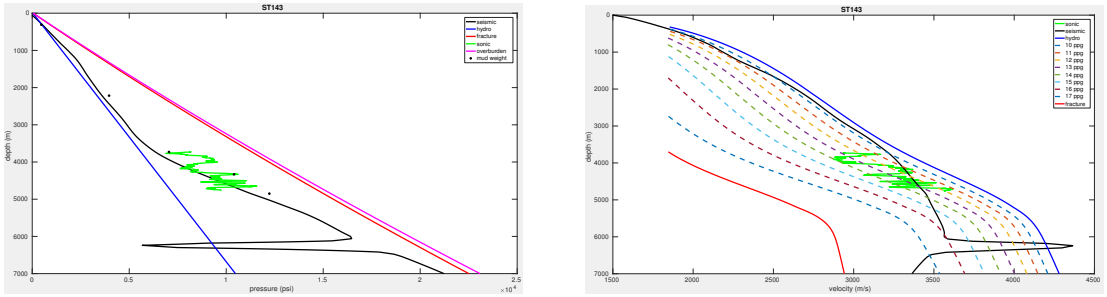

(a) (b)

Figure 12: Pore pressure profile (left) and velocity template (right) at well SS143. [**ER**]

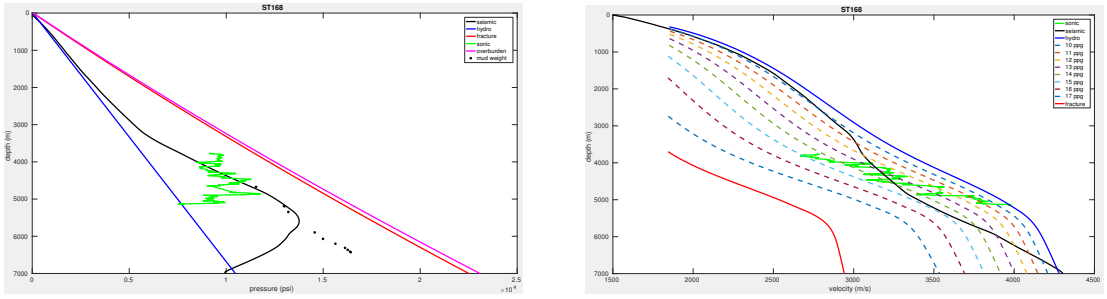

(a) (b)

Figure 13: Pore pressure profile (left) and velocity template (right) at well ST168. [**ER**]

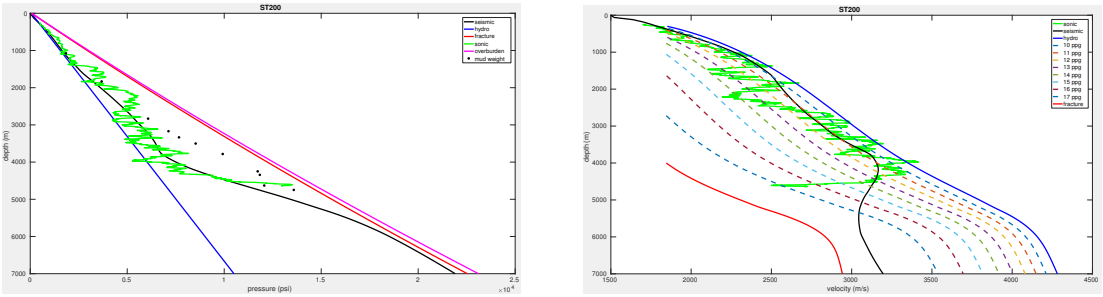

(a) (b)

Figure 14: Pore pressure profile (left) and velocity template (right) at well ST200. [**ER**]

REFERENCES

Bachrach, R., 2010, Applications of deterministic and stochasitc rock physics modeling to anisotropic velocity model building: SEG Annual International Meeting, Expanded Abstracts, 2436–2440, Society of Exploration Geophysicists.

Beardsmore, G. R. and J. P. Cull, 2001, Crustal heat flow: Cambridge University Press.

Dutta, N., B. Deo, Y. K. Liu, Krishna, Ramani, J. Kapoor, and D. Vigh, 2015, Pore-pressure-constrained, rock-physics-guided velocity model building method: Alternate solution to mitigate subsalt geohazard: Interpretation, **3**, SE1–SE11.

Dutta, N. C., 2002, Geopressure prediction using seismic data: Current status and the road ahead: Geophysics, **67**, 2012–2041.

———, 2016, Effect of chemical diagenesis on pore pressure in argillaceous sediment: The Leading Edge, **35**, 523–527.

Dutta, N. C., S. Yang, J. Dai, S. Chandrasekhar, F. Dotiwala, and C. V. Rao, 2014, Earth-model building using rock physics and geology for depth imaging: The Leading Edge, **33**, 1136–1152.

Issler, D. R., 1992, A new approach to shale compaction and stratigraphic restoration, Beaufort-Mackenzie basin and Mackenzie corridor, Northern Canada: AAPG Bulletin, **76**, 1170–1189.

Li, Y., B. Biondi, R. Clapp, and D. Nichols, 2016, Integrated VTI model building with seismic data, geological information, and rock-physics modeling-Part 1: Theory and synthetic test: Geophysics, **81**, C177–C191.

Matava, T., R. Keys, D. Foster, and D. Ashabranner, 2016, Isotropic and anisotropic velocity-model building for subsalt seismic imaging: The Leading Edge, **35**, 240–245.

Petmecky, R. S., M. L. Albertin, and N. Burke, 2009, Improving sub-salt imaging using 3d basin model derived velocities: Marine and Petroleum Geology, **26**, 457–463.